Ice Printer: Novel Method for Generating Impact Ice

Julia Feder,* Philip Thiele,† Patrick Meyer,‡ and Christian Hühne§
Technische Universität Braunschweig, 38106 Braunschweig, Germany

https://doi.org/10.2514/1.C038571

Aircraft icing poses a significant safety risk, making the replication of atmospheric icing conditions in a laboratory environment essential. Current ice generation methods for preliminary testing of ice protection systems primarily rely on silicon molds for static ice and icing wind tunnels for impact ice. However, due to the different freezing processes, static and impact ice differ, limiting the relevance of preliminary tests. This paper introduces a novel ice printer as a simplified method to generate impact ice on a small scale comparable to that produced in icing wind tunnels. For validation, ice specimens generated with the ice printer are compared to those from an icing wind tunnel and silicone molds. The comparison is based on optical properties, density, and adhesion strength measured via centrifuge testing. Results show that the ice printer can reproduce a range of icing conditions similar to those generated in icing wind tunnels, in terms of density and adhesion strength. The static ice specimens generated with silicon molds show similar density but slightly higher adhesion strength. Based on these findings, the ice generated with the printer can be classified as impact ice. Additionally, this novel method offers high reproducibility and significantly improves cost and time efficiency compared to traditional icing wind tunnels.

I. Introduction

THE formation of ice during flight poses major problems for aviation. Ice accumulation on aerodynamic surfaces, such as wings, alters the surface properties, increasing mass, drag, and local stalling, which significantly increases the risk of accidents and fuel consumption [1]. Another adverse effect of icing on aircraft structures is the change in lift behavior, as nonlinearities can occur in the lift curve at lower angles of attack [2]. Therefore, a reliable deicing or anti-icing system is essential for flight safety and is mandatory for aircraft operating in icing conditions [3].

According to the current state of the art, most passenger aircraft use thermal anti-icing systems, which use bleed air from the powertrain to heat critical structures such as slats [4,5]. However, ongoing research in aviation is increasingly focused on lightweight construction due to its potential to increase energy efficiency and reduce emissions from aircraft [6]. However, the carbon-fiber-reinforced polymers used for lightweight constructions are characterized by lower thermal conductivity and are less heat resistant than metallic materials [7], posing challenges for the use of existing anti-icing systems. A thermal anti-icing system based on bleed air can reach temperatures of several hundred degrees Celsius, jeopardizing the structural integrity of these components and thus increasing the risk of material damage. Given these technical challenges, it is clear that innovative ice protection technologies must be developed to ensure in-flight safety for future aircraft concepts.

Developing new ice-protection systems requires precise planning and comprehensive test procedures to ensure the effectiveness and reliability of the systems. For this purpose, fundamental test scenarios have been defined by the European Union Aviation Safety Agency and the Federal Aviation Administration, which include both laboratory and in-flight tests [1,8]. Crucial parameters for ice generation are stated to recreate the types of ice forming under atmospheric conditions as closely as possible, thereby obtaining meaningful results even in the early stages of development.

The main ice types occurring on aircraft under atmospheric conditions are rime ice and glaze ice. During rime ice formation, the droplet freezes instantly in its spherical form when hitting the surface, creating air-filled cavities in the ice. Because of the entrapped air, rime ice has a white, rough surface and a smaller density than glaze ice [9]. Because of the almost instantaneous freezing of the impinging water droplets, rime ice accumulation closely follows the original structure's shape, reducing the aerodynamic performance drawbacks [10]. Suppose the convective heat flow during phase transformation is not high enough, the phase transformation of the droplet is delayed, and the water runs along the surface before freezing completely. This so-called *wet growth* results in a smooth, transparent layer of glaze ice with no entrapped air [11]. Glaze ice accretions drastically change airfoil shape, resulting in large regions of flow separation and, therefore, severe drag rise [12]. It has a higher density than rime ice and is favored by larger droplets and temperatures near the freezing point. In some cases, both growing types can occur on the same structure, forming mixed ice [13].

Temperature-controlled icing wind tunnels produce these different ice types in a representative and reproducible way and investigate the accretion of impact ice on surfaces. The adjustable parameters depend on the specific icing wind tunnel and its spraying device. They typically include the droplet size and distribution, ambient and water temperature, and water and airflow rate. Using specific nozzle systems, various forms of ice growth, such as glaze, rime, and mixed ice, can be generated under simulated atmospheric conditions. Various icing wind tunnels of different sizes and adjustment parameters can be found in the literature [14–17].

Although icing wind tunnels are essential for certifying new ice-protection systems, their use involves certain disadvantages, especially in the early stages of development. One disadvantage is the limited comparability of the produced ice layers with other icing wind tunnels due to the various adjustable parameters [18]. Icing wind tunnels are also not available in many laboratories due to high maintenance and operational costs and the need for expensive peripheral equipment. In addition, implementing realistic test scenarios in an icing wind tunnel requires time-consuming and cost-intensive preparation. For these reasons, more straightforward methods of ice production are often used for preliminary tests on subcomponents.

Ice formation without the use of an icing wind tunnel is commonly achieved through spray bottles, freezing molds, or cold chambers equipped with spray nozzle systems. In the spray bottle approach, distilled water is manually applied to the specimen within a cold environment, causing the droplets to freeze upon impact.

Received 16 May 2025; accepted for publication 21 September 2025; published online 31 October 2025.

*Research Associate and Doctoral Student, Institute of Mechanics and Adaptronics, Langer Kamp 6; j.feder@tu-braunschweig.de. Joint first author (Corresponding Author).

†Research Associate and Doctoral Student, Institute of Mechanics and Adaptronics, Langer Kamp 6; philip.thiele@tu-braunschweig.de. Joint first author.

‡Postdoctoral Research Associate, Institute of Mechanics and Adaptronics, Langer Kamp 6; pat.meyer@tu-braunschweig.de.

§Professorship for Function Integration, Institute of Mechanics and Adaptronics, Langer Kamp 6; christian.huehne@tu-braunschweig.de.

Because freezing is initiated by the collision of supercooled droplets with the surface, the resulting ice is referred to as impact ice. A more controlled method involves cold chambers with atomizing nozzles, which produce a uniform spray of fine droplets that impinge on the surface and freeze similarly to form impact ice [19]. In contrast, the freezing process of static ice is triggered by the cooling of water, which causes the ice layer to form from the edge to the center, resulting in high air entrapment [20]. For static ice generation, a freezing mold is placed on the surface, filled with distilled water, and put in a freezer. This method is straightforward to handle and non-time-consuming and allows different shapes of static ice to be generated. However, static ice shows severe differences from impact ice. Tetteh et al. [21] compare static ice's adhesion strength with impact ice produced in an icing wind tunnel and shows a 45% higher shear adhesion strength for static ice than impact ice when using metal substrates. Other studies show similar differences in tensile adhesion strength when comparing impact ice and static ice [22,23].

The previously mentioned reasons highlight some limitations of current ice-generating methods in recreating impact ice on a small scale and the resulting reduced significance of preliminary tests for deicing and anti-ice systems. Hence, this paper introduces a novel ice printer that generates impact ice while avoiding costly and time-consuming tests in icing wind tunnels. Combining the mechanics of a three-dimensional (3D) printer with a two-component jet nozzle, the variety of adjustable parameters enables the fast generation of ice similar to that of an icing wind tunnel for preliminary tests of ice protection systems on a small scale in early development stages of deicing and anti-icing systems.

The paper is structured as follows. The setup and working principle of the novel ice printer are introduced in detail in Sec. II. As the paper aims to classify the printer as a method for impact ice production in the early development stages of ice protection systems, the results must be compared with state-of-the-art ice-generating methods. Therefore, the ice layers generated with the ice printer are compared with those generated with an icing wind tunnel and silicone molds. The parameters used to generate the ice layers of the different ice types with each method are presented in Sec. III. The density, adhesion strength, and optical properties of the produced ice are used to compare the different ice-generating methods with each other. The results of these measurements are presented in Sec. IV and discussed in Sec. V. A conclusion and an outlook on the topic are given in Sec. VI.

II. Novel Ice Printer

The ice printer is designed to produce glaze and rime ice comparable to that produced in an icing wind tunnel. However, the ice printer is much smaller and simpler to use, which allows it to be operated in a regular household freezer. This ensures precise control of the ambient temperatures below the freezing point. The system includes extended printer electronics and pneumatic control loops to create a controlled water spray through a two-component nozzle, applied in layers to a substrate. Ice layers can be applied to individual geometries due to the relative movement between the nozzle and the substrate.

Figure 1 shows the freezing process of water and the functional principle of the ice printer adapted to the freezing process. The water is precooled in a tank to just above the freezing point. The water is channeled to the nozzle, while the water temperature is still over 0°C. Behind the nozzle outlet, the water continues to cool down, and the resulting droplets supercool in the air between the nozzle outlet and the substrate. The supercooling of the liquid water causes immediate freezing of the droplets upon impact with the test specimens. To ensure the complete freezing process of each layer, localized areas are wetted only for a limited time.

Figure 2 shows the main components of the ice printer involved in the ice printing process. This section provides a detailed explanation of each component and its function. Additionally, the key parameters influencing the printing process and their corresponding technical ranges are discussed.

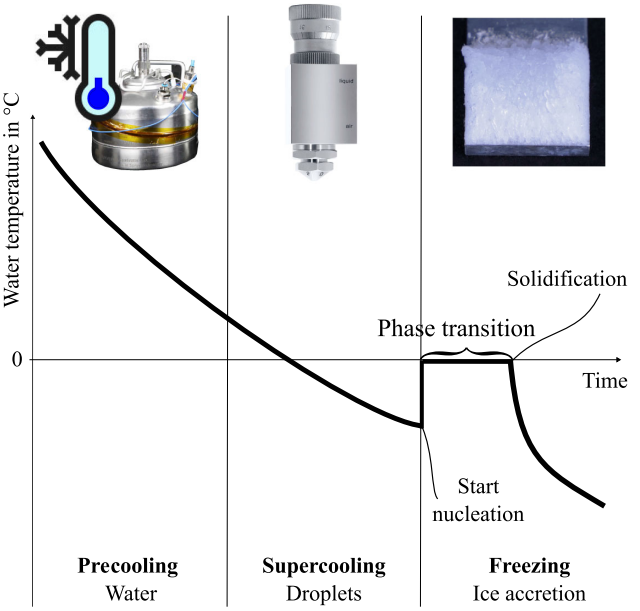

Fig. 1 Schematic principle of ice production using the ice printer.

A. Setup and Main Components of Ice Printer

The system consists of the kinematic components and the associated electronics of a 3D printer, which is extended by heating components, a two-component nozzle, pneumatic control loops, and a water tank (see Fig. 2). The central component of the ice printer is an external-mix two-component nozzle (Schlick model 970 S8), which can adjust droplet size and volume flow ratio of water to air. The nozzle generates a cloud of water droplets with a diameter of 10 to 50 μm. It is mounted on the carriage of the computerized numerical control (CNC) kinematics of the 3D printer (Anycubic i3) with a moving printing bed. The maximum icing area is 200 mm $\times$ 200 mm, defined by the size of the printing bed. In this study, only flat test specimens have been frozen and used for further experiments, which fit on the printing bed. It is conceivable to ice more complex geometries, such as airfoil profiles, as long as the distance between the surface and the nozzle outlet remains large enough. The triaxial control enables the measurement of elevation profiles for various sample geometries, using an installed tactile sensor (Geeetech 3Dtouch V3.2) with an accuracy deviation of 0.005 mm. Measuring the specimen elevation in the original and iced states before and after ice printing at predetermined points allows the determination of the ice-layer thickness. Knowledge of the ice height enables the characterization of the printed ice. The required water for printing different ice layers is stored in a water tank, where it is precooled to 2°C before the printing process begins. An insulated tube connects the nozzle to the tank.

Most electronic and pneumatic components are outsourced from the freezer in an extra box (see Fig. 3). The entire system is controlled via the printer's original mainboard. The printer's power supply is the primary power source. Unused pins and connections are assigned to the additional components that have been installed. Two heating bands regulated by the adapted proportional-integral-derivative (PID) heating control of the printer are installed on the tank and the water tube to prevent the water from freezing in the individual components. The heating bands are interfaced with the printer's existing heating ports, replacing the original heating elements of the print bed and extruder. The original temperature sensors have been replaced with temperature sensors with cartridges. They are installed in the tank and the tube near the nozzle to implement two water temperature control loops.

The in-house air supply, equipped with two downstream pressure regulators, is used for regulating both water and air pressure. The air pressure regulators are connected to the I^2C pins via digital-to-analog converters (DACs) in between. An additional 12 V supply is installed for the pneumatic components. The first regulator

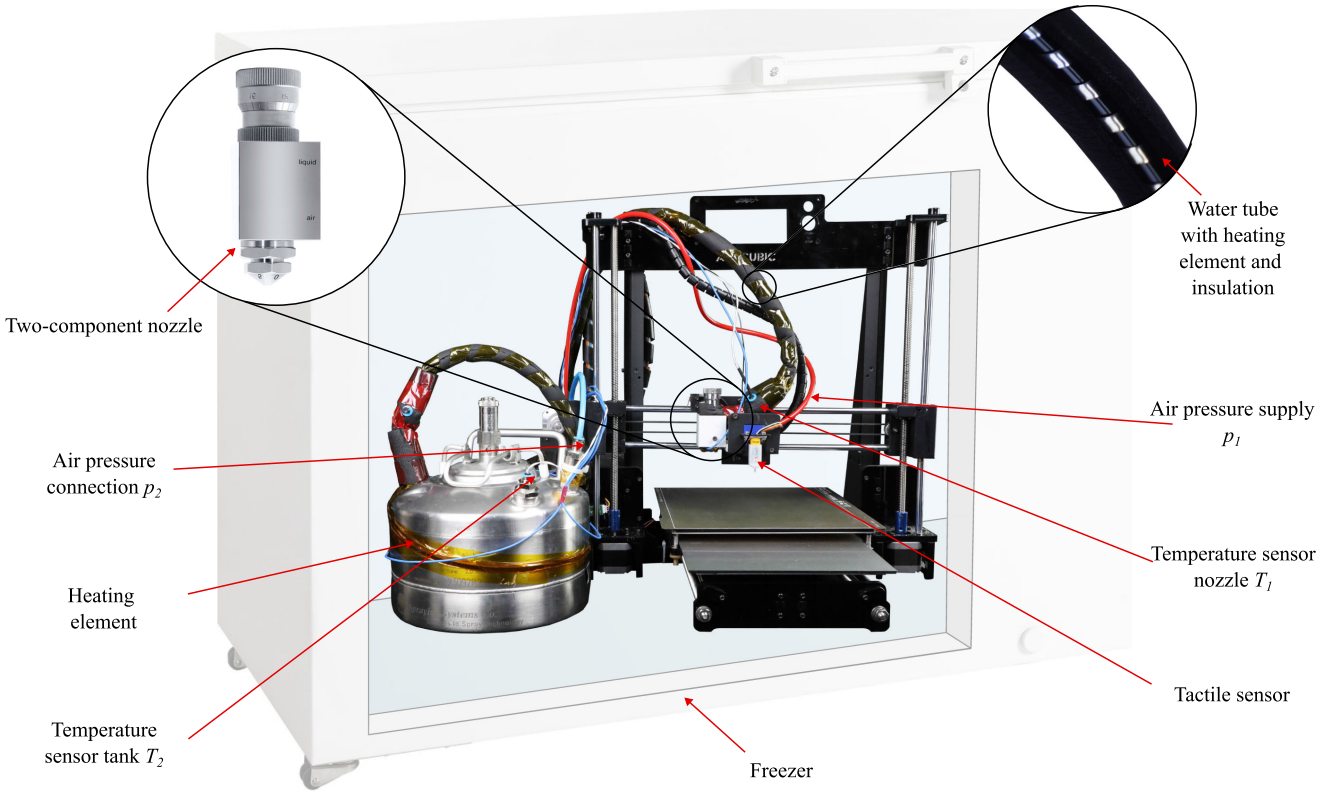

Fig. 2 Setup of the ice printer with its main components operating in a freezer.

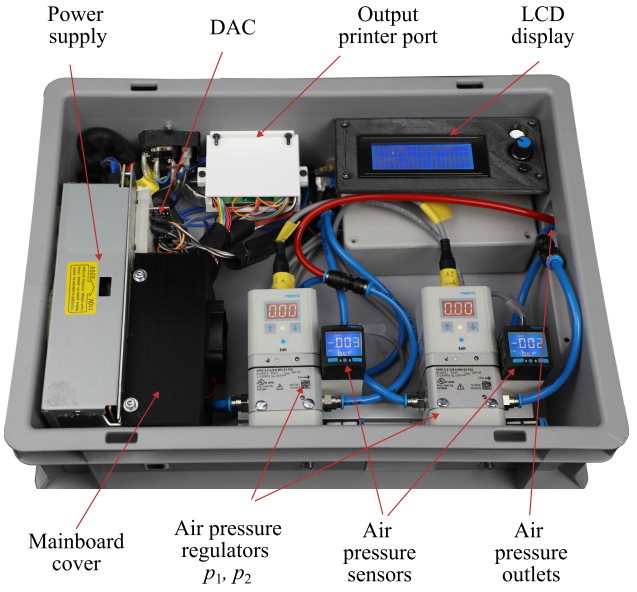

Fig. 3 Electronic and pneumatic components of the ice printer.

directly adjusts the air pressure at the nozzle, whereas the second pressurizes the water tank, generating a water volume flow to the nozzle. Additionally, two pressure sensors are installed for precise monitoring. Figure 4 shows the ice printer's different circuits, including the heat, the air, the water, and the information flow.

All components are controlled by custom Marlin firmware, which was modified to meet new requirements and support additional functionality. In the first step, the existing firmware was adapted to the new environment; for example, the parameters of the PID control were tuned to accommodate the new heating elements. In the second step, new G-code commands were implemented to enable control of additional components such as the pressure regulators. All G-code commands are transmitted to the printer via G-code files. These files define the printing process parameters, including the geometry and positioning of the test specimen, as well as the ice type and thickness. By optimizing the spacing between parallel printed ice lines within a single layer and varying the orientation of stacked layers, a homogeneously distributed ice layer can be applied to the test specimen. The files also specify the coordinates of the ice-layer height measuring points used to characterize the test specimens. The printing process is started and monitored via Pronterface.

B. Parameter Range and Adjustments

Conditions similar to those in an icing wind tunnel can be simulated by adjusting the air and water pressure at the two-component nozzle, the ambient conditions, and printing parameters, enabling the generation of different ice types. The adjustable parameters are summarized in Table 1. The possible ranges of the median volume diameter (MVD) and mass flow rate, which depend on the nozzle model, are also listed. The settings used for the desired spray patterns were extracted from the nozzle data sheet. No measurements were taken to determine the nozzle-specific parameters. Further information can be taken directly from the data sheet.¶

The freezing process is strongly influenced by water and ambient temperatures, which are key parameters that govern droplet supercooling. The water in the tank must be precooled to just over 0°C. Low ambient temperatures allow droplets to supercool before hitting the specimen surface. Figure 5 visualizes the supercooling of droplets a few centimeters behind the nozzle outlet. In general, lower temperatures are more beneficial for the accretion of rime ice, while higher temperatures near 0°C slow the freezing process and promote the growth of glaze ice.

The pressure regulators apply air pressure to the nozzle and the water tank, mainly controlling the water mass flow and the MVD.

¶Information available online at https://cdn.sanity.io/files/63o789br/production/627e43176aec1c1db74942ca0f20c4f9da3df06e.pdf [retrieved 7 May 2025].

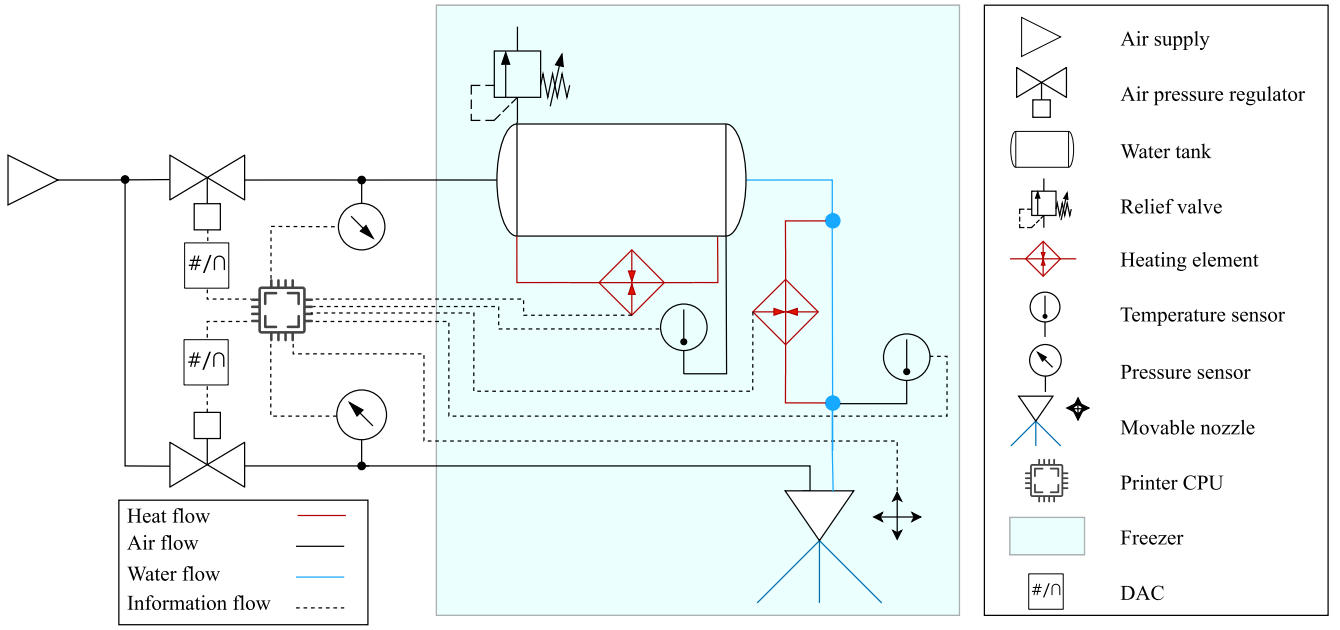

Fig. 4 Pneumatic and electronic circuits of the ice printer.

Table 1 Parameter range for the printing of different ice types

Parameter	Possible range	Used range
Ambient temperature T_1, °C	−20 to 0	−15 to −5
Water temperature T_2, °C	0 to 20	0 to 2
Air pressure p_1, bar	0.3 to 6.0	0.3 to 0.6
Water pressure p_2, bar	0.3 to 6.0	0.6 to 0.8
Water regulation needle setting	1 to 7	4
Nozzle height h, mm	0 to 200	30 to 70
Nozzle speed v, mm/ min	0 to 10,000	2000 to 6000
Water mass flow $\dot{m}$, g/s	0.01 to 23.75	0.05 to 0.17
MVD, μm	10 to 50	20 to 40

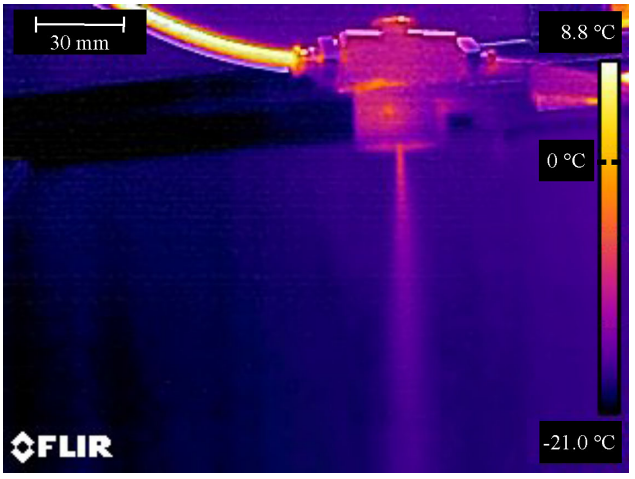

Fig. 5 Thermal image of supercooling droplets behind the nozzle outlet.

The flow rate determines the local amount of water on the test specimen, which is primarily regulated by the tank pressure. In contrast, the injector effect due to higher air pressure at the nozzle has a minimal impact on it. An increase in air pressure results in stronger water suction due to the resultant negative pressure at the nozzle outlet. Although this effect has minimal impact on the mass flow, the air pressure at the nozzle can control the MVD distribution and the velocity of the outflowing water droplets. Because of the external mixing principle of the two-component nozzle used, the decay of the water jet in single droplets occurs behind the nozzle outlet and is influenced by the airflow within the nozzle. To summarize, a higher water volume flow rate benefits the generation of glaze ice, whereas lower flow rates favor rime ice. Higher air pressure at the nozzle results in a lower MVD, which is beneficial for rime ice. However, the maximum air pressure is limited to 1 bar because pretests have shown a high reflection of droplets from the surface for higher pressures. The minimum water pressure is limited to 0.3 bar to ensure a sufficient water flow rate to prevent freezing of the nozzle.

The nozzle allows fine-tuning of the water flow rate via an integrated water regulation needle. The needle allows adjustment of the water-to-air flow ratio without changing the air and water pressures. Pretests have shown that both ice types can be produced with the regulation needle set in position 4. To automate the printing process, the nozzle is used with this setting permanently, while the other parameter can be automatically adapted to the needs of the ice type.

The nozzle height and thus its distance from the test specimen affect the local water deposition on the substrate, the width of the printed paths, and consequently, the available time for droplet supercooling. This height can be precisely adjusted using the printer's CNC kinematics. The supercooling of the droplets depends on the time they interact with the surroundings between the nozzle and the specimen surface. An increased nozzle height results in lower droplet temperatures, while simultaneously reducing the local water amount on the specimen surface. This reduces the heat that needs to be dissipated and the thickness of each printed layer, which is advantageous for rapid heat dissipation. Figure 6 shows the development of the wetting diameter d depending on the nozzle height h. The theoretical spray angle of $\varphi = 40°$ is valid only up to a nozzle height of $h = 70$ mm, beyond which the wetting diameter remains constant at approximately $d = 51$ mm. To generate homogeneous ice layers, the height-dependent wetting diameter has to be considered in the G-code by adjusting the spacing between parallel lines. In summary, a higher nozzle height is favorable for generating rime ice due to the associated lower droplet temperatures and a smaller amount of heat that has to be dissipated.

The nozzle's movement speed can be varied to regulate the amount of water deposited per area on the specimen surface. A faster nozzle movement leads to a smaller water volume and, consequently, less heat that must be dissipated. However, the nozzle

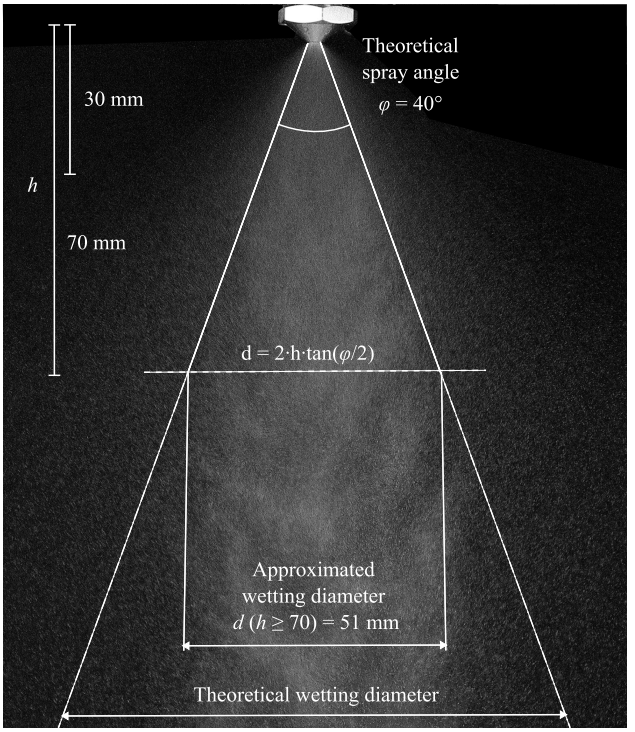

Fig. 6 Comparison of theoretical and experimental wetting diameter.

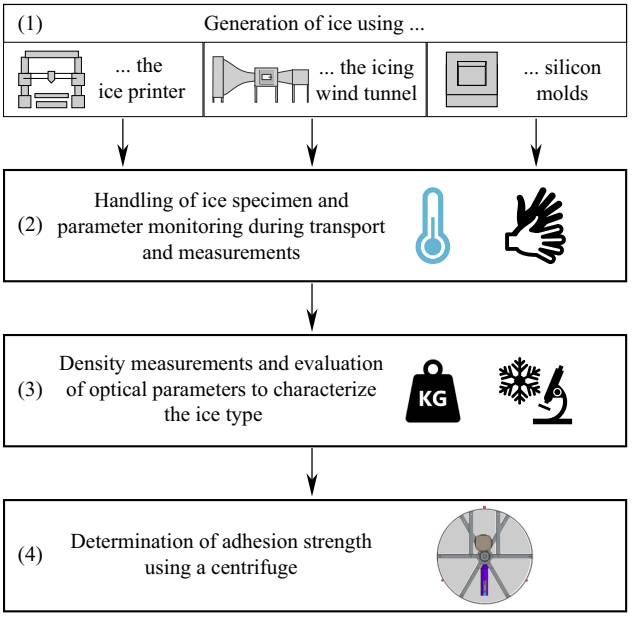

Fig. 7 Workflow of the ice generation and characterization process using the ice printer, icing wind tunnel, and silicon molds.

speed is subject to certain limits. A speed above 6000 mm/min causes abrupt and sudden nozzle movements, resulting in unstable spray patterns. Conversely, a lower limit of 2000 mm/min was experimentally evaluated and is a good compromise between water quantity and the time needed to produce a single layer. Therefore, higher nozzle speeds are advantageous for producing rime ice, whereas lower speeds are used for glaze ice. With appropriate parameter settings, the printer is capable of producing both glaze and rime ice, establishing this compact and cost-efficient method as a viable alternative for fundamental research on deicing and anti-icing systems.

III. Methods for Generation and Characterization of Rime and Glaze Ice

To evaluate the ice generated by the ice printer, it is compared to reference specimens generated with an icing wind tunnel and via static freezing in silicon molds. The underlying assumption is that the ice generated with the ice printer more closely resembles impact ice from the icing wind tunnel than static ice from the silicon molds. A comprehensive characterization of atmospheric ice can be based on a variety of parameters, including optical appearance, density, adhesion strength [24], compressive strength [25], tensile strength [25,26], and elastic modulus. These parameters vary significantly depending on the ice type and environmental conditions and collectively provide a detailed profile of the ice's mechanical and physical behavior. In the present study, however, the characterization is limited to optical properties, density, and adhesion strength. These three parameters were selected due to their practical accessibility in the given experimental setup and their proven ability to provide meaningful insight into the structural and functional characteristics of different ice types. More advanced mechanical parameters, such as tensile or compressive strength and Young's modulus, while valuable, require significantly more complex setups and are therefore considered beyond the scope of this initial investigation.

The ice layers are generated on rectangular aluminum specimens measuring 150 mm × 20 mm with a thickness of 2 mm. The area for ice accumulation is at the tip of the specimen and measures 20 mm × 20 mm. These dimensions were chosen to ensure that the contact area between the ice and the specimen exceeds the required minimum of 10 mm × 10 mm [27,28]. The specimens are precooled before ice generation for all methods to minimize temperature gradients between ice and specimen, thereby reducing the risk of interfacial fracturing caused by thermal strain [11].

Figure 7 provides a graphical overview of the experimental workflow. Accurate specimen handling and precise control of process parameters are essential to ensure reproducible and reliable results, as previous studies have shown that environmental and procedural factors can significantly affect ice adhesion strength [27]. Among these, temperature has been identified as the most critical parameter influencing adhesion, not only during ice formation [29] but also throughout the testing process [23,30]. Consequently, temperatures were carefully monitored during both freezing and testing phases. To prevent premature melting and refreezing at the interface, which could alter adhesion characteristics, all frozen specimens were handled with gloves to minimize heat transfer.

A. Parameters Used for Ice Generation

Depending on parameters such as ambient temperature, liquid water content (LWC), droplet size, wind speed, and others, the generation of either rime ice or glaze ice is favored. Politovich [31] states that on airframe structures rime ice production is favored by ambient temperatures below −10°C, a LWC of 0.15 g/m^3 to 50.38 g/m^3, and droplets with a small MVD. Conversely, larger droplets, higher airspeed, and temperatures near the freezing point favor the formation of glaze ice. Based on these observations, production parameters are determined to generate rime and glaze with the ice printer and the icing wind tunnel. For all methods, an ice mass of 1 g is aimed for during ice generation.

When generating different ice types with the ice printer, parameter values comparable to those reported in the literature for other ice-generation methods are targeted. Because the parameters LWC, wind speed, and MVD cannot be controlled directly with the ice printer, process parameters such as water pressure, air pressure, nozzle speed, and nozzle height are adjusted to influence them indirectly. To achieve a low LWC, the water pressure is reduced to limit the water flow rate. The wetting of the specimens is controlled by adjusting the nozzle speed and height. Higher nozzle height and speed decrease the wetting of the specimen and thus the LWC. A higher nozzle height and low ambient temperatures promote droplet supercooling before they hit the test specimen. The specific parameter sets used for rime ice and glaze ice production with the ice printer are listed in Table 2.

Table 2 Parameters used for rime and glaze ice production with the ice printer

Parameter	Rime ice	Glaze ice
Ambient temperature T_1, °C	−15	−10
Water temperature T_2, °C	0	0
Air pressure p_1, bar	0.6	0.3
Water pressure p_2, bar	0.6	0.8
Water regulation needle setting	4	4
Nozzle height h, mm	70	30
Nozzle speed v, mm/s	6000	2000
Water mass flow $\dot{m}$, g/s	0.09	0.12
MVD, μm	20 to 40	20 to 40

The icing wind tunnel of the Institute of Mechanics and Adaptronics at Technische Universität Braunschweig is used in this study to generate reference rime and glaze ice specimens. It consists of an open-return wind tunnel (Eiffel-type) located within a large freezer chamber, which enables the controlled simulation of atmospheric icing conditions. The spray bar system of the icing wind tunnel consists of three bars with five nozzles each. Hydraulic atomizing nozzles of the type PJ6, manufactured by BETE Fog Nozzle, are used. Depending on the water pressure, droplets with an MVD of 40 to 90 μm are created.[**] The droplets supercool on their way to the test section and form an ice layer upon impact on the surface of the test specimen. A detailed description of the icing wind tunnel, depicted in Fig. 8, can be found in Ref. [17].

Different parameters can be adjusted to generate the desired ice type. The MVD inside the icing wind tunnel is determined by the adjustable water pressure p and can be calculated by

$$\mathrm{MVD} = 85.77\ \mu\mathrm{m}\left(\frac{p}{\mathrm{bar}}\right)^{-0.326} \tag{1}$$

The LWC inside the test section depends on the number of active nozzles n and the wind speed v used for ice production and can be calculated by

$$\mathrm{LWC} = \frac{n\dot{m}}{vA_{\mathrm{wt}}} \tag{2}$$

in which $A_{\mathrm{wt}} = 0.45\ \mathrm{m} \times 0.45\ \mathrm{m}$ is the cross-section of the wind-tunnel test section and $\dot{m}$ is the mass flow of the water. The mass flow is given as a function of pressure by the manufacturer of the nozzles and is calculated by

$$\dot{m} = 0.228\ \mathrm{g/s}\sqrt{\frac{p}{\mathrm{bar}}} \tag{3}$$

The parameters used to produce rime and glaze ice with the icing wind tunnel in this study are listed in Table 3.

As a third method for ice generation, static ice is produced by filling silicone molds with distilled water. Each mold is filled with 1 mL of distilled water to form approximately 2.5 mm thick ice layers. For freezing, the molds are placed inside a freezer at an ambient temperature of −10°C for 24 h to ensure the complete solidification of the ice.

Figure 9 presents the ice layers generated by the three different methods. From left to right, the figure shows static ice formed in the freezer, glaze ice generated with the ice printer and the icing wind tunnel, and rime ice generated with the icing wind tunnel and the ice printer. The glaze ice specimens exhibit smooth, mostly transparent surfaces. Similarly, the static ice also appears smooth but is more opaque due to air entrapment during the freezing process. Glaze ice samples created with both the printer and wind tunnel show slight overhangs along the sides and top of the specimens. As these overhangs are not connected to the specimen edges, they are disregarded in the calculation of the adhesion strength. The rime ice specimens show a rough, white surface, resulting from the immediate freezing of supercooled droplets upon impact and a high air content within the ice structure. The rime ice generated with the ice printer appears rougher than that produced in the icing wind tunnel, with more prominent accumulations of individual ice crystals. This difference may be attributed to the difference in droplet size between the two methods. The specimens were evaluated solely based on surface characteristics; no cross-sectional analysis was conducted to assess the homogeneity of the ice layer.

B. Methods for Ice Characterization

Density and adhesion strength measurements are conducted to identify and compare the ice layers generated using different methods. Density values are used to distinguish between rime ice and glaze ice. Because of the amount of entrapped air, rime ice shows lower density values than glaze ice. The literature reports density values from 0.28 to 0.89 g/cm^3 for rime ice, depending on impact velocity and ambient temperature [32,33]. Glaze ice typically exhibits slightly higher density values, with the literature reporting values ranging from 0.86 to 0.90 g/cm^3 [33]. Similar values are reported for static ice [24].

The ice density ρ is calculated using Eq. (4), as the ratio of the ice mass m to the volume V of the ice layer. The volume is obtained by multiplying the contact area between the ice and the test specimen by the layer's thickness. The ice thickness is measured using the tactile sensor integrated into the ice printer, with the average value derived from 36 measurement points. The ice mass is determined using the precision scale "KERN 572-30" by KERN and SOHN, GmbH,[††] which is designed for ambient temperatures down to −10°C,

$$\rho = \frac{m}{V} \tag{4}$$

Adhesion strength measurements are conducted because adhesion strength is a crucial parameter in evaluating deicing systems. To validate the ice printer as a viable method for generating impact ice without using an icing wind tunnel, the adhesion strength of the printed ice should closely match that of ice produced in the wind tunnel. Achieving comparable values enhances the reliability of the ice printer as a novel method for producing representative ice layers, thereby increasing the significance of test results during the early development stages.

Standard methods for quantifying ice adhesion include centrifuge testing and direct mechanical testing. According to Bleszynski and Clark [34], mechanical testing can be further subdivided into horizontal shear, vertical shear, and tensile tests, depending on the direction and mode of applied load. Because of the fixed test setups in mechanical testing machines, posttest inspection of the ice-substrate interface is typically feasible, enabling detailed failure analysis. In centrifuge testing, the specimen is mounted on a rotating arm within a cold room and subjected to increasing angular velocity until the resulting centrifugal force overcomes the adhesive bond. This method is characterized by high efficiency, consistency, and repeatability [30]. For an in-depth discussion of various adhesion test methodologies and their applicability, the reader is referred to the reviews by Makkonen [11], Kasaai and Farzaneh [35], and Rønneberg et al. [27]. In the present study, centrifugal adhesion testing is employed to evaluate the adhesion strength of the ice samples.

[**]Information available online at https://bete.com/wp-content/uploads/2022/01/BETE_PJ-metric.pdf [retrieved 7 May 2025].

[††]Information available online at https://www.kern-sohn.com/cosmoshop/default/pix/a/media/T572-30-A/TD_572-30_de.pdf [retrieved 7 May 2025].

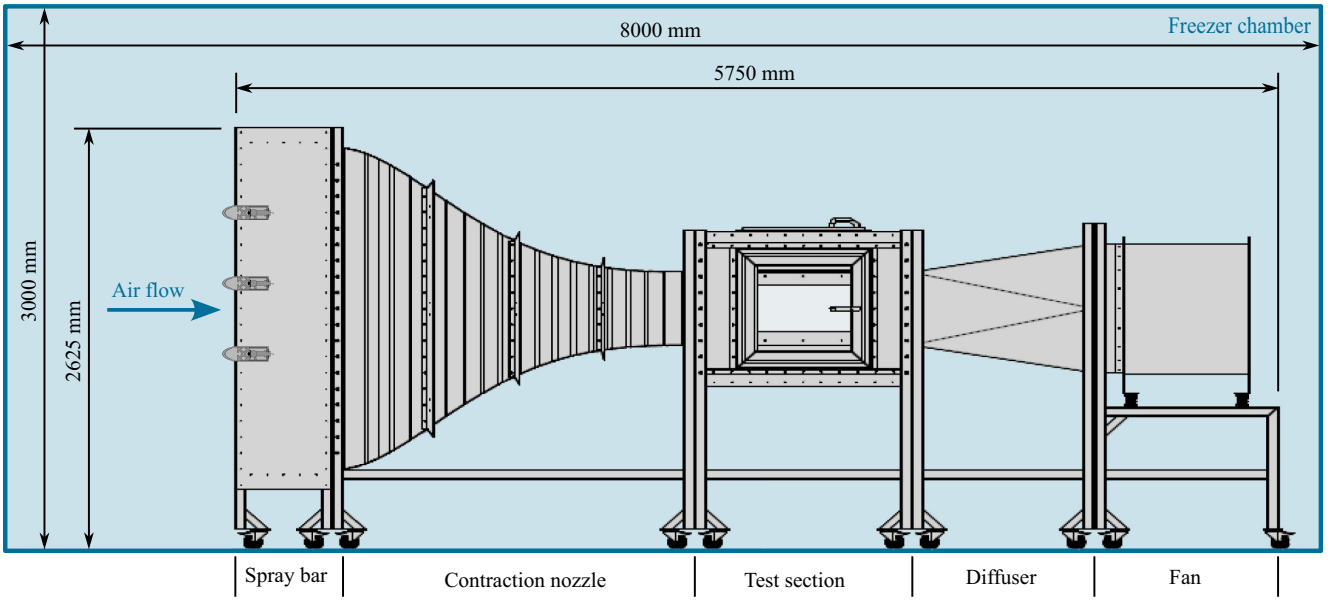

Fig. 8 Deicing test facility of the Institute of Mechanics and Adaptronics at Technische Universität Braunschweig [reprinted from Ref. [17] with permission from ASCE (copyright 2023, ASCE, American Society of Civil Engineers)].

Table 3 Parameters used for rime and glaze ice production in the icing wind tunnel

Parameter	Rime ice	Glaze ice
Ambient temperature T_1, °C	−17	−5
Air speed v, m/s	29.7	27.1
Number of nozzles n	2	6
Spray time, s	360	120
Water mass flow $\dot{m}$, g/s	0.46	0.40
MVD, μm	55	59
LWC, g/m^3	0.12	0.44

Adhesion tests are carried out with the centrifuge of the Institute of Mechanics and Adaptronics at Technische Universität Braunschweig [36], shown in Fig. 10. The centrifuge rotor has a radius of 250 mm and is designed for a maximum rotational speed of 9000 1/min. Three acceleration sensors are placed inside the centrifuge, each covering 120° of the radius and measuring the impact of shedding ice. Two additional sensors measure the rotational speed of the rotor. The centrifuge is stationed inside a freezing chamber to hold a constant ambient temperature of −10°C during testing, as the literature shows increased adhesion strength for decreasing temperature during testing, especially when reaching temperatures below −12°C [23,30].

For testing, the specimens are mounted at the end of the rotor arm, and the measurement is started. An acceleration of 200 1/min/s is used to reach a maximum rotational speed of $\omega = 4000$ 1/min. The shear stress τ acting on the ice layer is calculated by dividing the force F acting on the ice mass by the contact area A between the ice and the substrate. The force F can be expressed as a function of the ice mass m, the radial distance r from the axis of rotation to the center of the icing area, and the rotational speed ω. Figure 10 depicts the centrifuge setup and relevant parameters. With the used setup, only the maximum adhesion strength τ_{max} can be measured, which corresponds to the shear stress at break, calculated using Eq. (5):

$$\tau_{max} = \frac{F_{max}}{A} = \frac{mr\omega_{max}^2}{A} \tag{5}$$

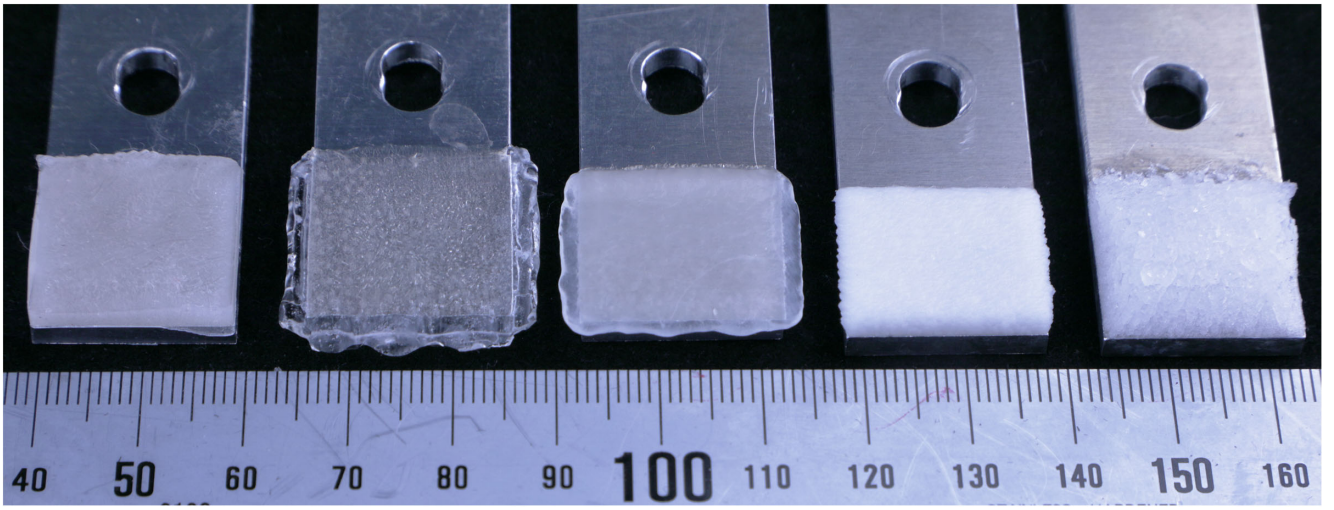

Fig. 9 Ice generated with different methods. Left to right: static ice (freezer), glaze ice (ice printer and icing wind tunnel), rime ice (icing wind tunnel and ice printer).

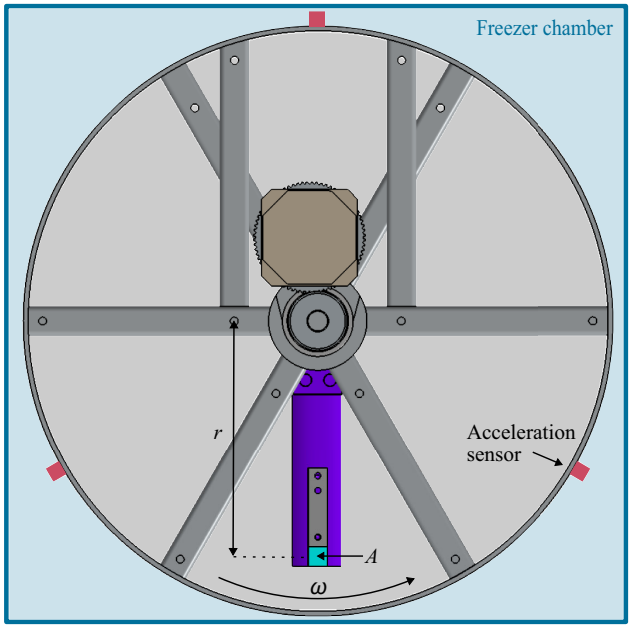

Fig. 10 Centrifuge used for adhesion strength measurements.

IV. Results of Density and Adhesion Strength Measurements

Density measurements indicate that the values of the generated ice specimens are similar to those reported in the literature for rime and glaze ice [32,33]. The static ice generated in the freezer shows a density of 0.89 g/cm^3, the same as the glaze ice generated with the ice printer. The density of the glaze ice generated in the icing wind tunnel is slightly higher, with a value of 0.94 g/cm^3. Rime ice specimens have a lower density due to the entrapped air during the freezing process. For the icing wind tunnel, the generated rime ice specimens have a density of 0.75 g/cm^3, while the rime ice generated with the ice printer shows a value of 0.74 g/cm^3. Table 4 summarizes the results of the density measurements for all ice-generating methods.

The adhesion strengths measured for the different ice types and generation methods are presented as box plots in Fig. 11. In the box plot, the central box represents the range of values from the lower to the upper quartile. The horizontal line inside the box represents the mean value of the data points. The whiskers extend to the smallest and highest data points that are not considered outliers. The outliers are shown as separate points in the diagram and classified as such if they lie outside 1.5 times the interquartile range.

The data points for both rime ice measurement series fall within a comparable range. The lowest adhesion strength is measured for rime ice produced in the icing wind tunnel, with a mean value of 50 kPa. The whiskers extend from 38 to 63 kPa, and the narrow box and short whiskers indicate low variability in the measurements. Rime ice generated by the ice printer shows a slightly higher mean adhesion strength of 66 kPa, accompanied by a larger box and wider whiskers, indicating a higher data variability.

The glaze ice specimens also show consistency between the different generating methods and exhibit slightly higher adhesion strength values compared to rime ice. The lowest mean value of 69 kPa is observed for glaze ice produced in the icing wind tunnel. This data set shows considerable variability, with whiskers extending from 46 to 97 kPa, and a single outlier measured at 107 kPa. Comparable results are obtained for glaze ice produced with the ice printer, showing a mean adhesion strength of 75 kPa, and whiskers extending from 54 to 106 kPa.

The adhesion strength measured for static ice produced with silicon molds in the freezer is slightly higher than that of glaze ice. The measured mean value is 82 kPa, with the whiskers extending from 77 to 89 kPa. An additional outlier is recorded at 94 kPa.

Table 4 Density values of the specimens generated with the ice printer, the icing wind tunnel, and the freezer

Generating method	Type of ice	Density value in g/cm^3
Freezer	Static ice	0.89
Ice printer	Glaze ice	0.89
Icing wind tunnel	Glaze ice	0.94
Icing wind tunnel	Rime ice	0.75
Ice printer	Rime ice	0.74

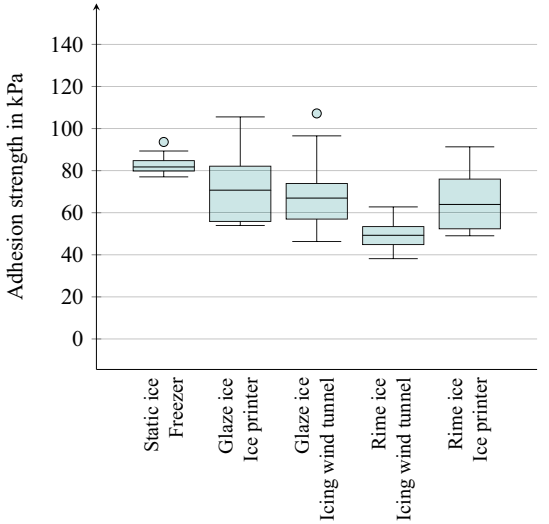

Fig. 11 Comparison of the adhesion strength of different ice types generated with the icing wind tunnel, the ice printer, and the freezer.

V. Discussion

The optical properties of the ice specimens shown in Fig. 9 and the density values listed in Table 4 indicate that the desired ice types were successfully generated with each method. Glaze ice specimens show a measured density of 0.89 to 0.94 g/cm^3, depending on the generating method. Similar values are measured for static ice generated in silicon molds. Rime ice specimens show lower densities than glaze and static ice and range from 0.74 to 0.75 g/cm^3, depending on the generating method. For all ice types, the measured densities are consistent with values found in the literature [32,33]. Notably, the measured adhesion strength values presented follow a trend that aligns closely with the density distribution, suggesting that density may play a more significant role in characterizing ice behavior than a purely visual classification. This observation is supported by recent studies, which propose a density-based framework for distinguishing between ice types and correlating their mechanical properties [37]. Palanque et al. [38] proposed a continuous description of ice based on density, demonstrating that parameters such as Young's modulus and fracture toughness correlate more strongly with density than with visual classification. Their findings support the hypothesis that density serves as a key parameter in interlaboratory comparisons and material characterization. In light of this, the present study emphasizes density as a central parameter for comparing ice types and interpreting adhesion strength measurements. The observed discrepancies in adhesion strength (particularly between rime ice samples of similar density) further suggest that the underlying structure and formation history may play a larger role than previously assumed and that the density-based approach provides a more robust framework for ice classification.

Comparing the adhesion strength measurements of glaze ice generated with the ice printer and icing wind tunnel supports the assumption that both methods generate similar ice structures. Both show mean adhesion strength values around 70 kPa, along with comparable density values and optical properties, indicating that the ice printer successfully produces impact ice. Furthermore, the

adhesion strength of glaze ice from both the ice printer and the icing wind tunnel is lower than that of static ice generated in the freezer. This aligns with literature findings [22,39] and further supports the classification of printer ice as impact ice. Tetteh et al. [21] attribute the higher adhesion strength of static ice to the uniformity of its freezing process, leading to a more consistent crystalline bond, whereas impact ice forms through the accumulation of multiple freezing events. Another explanation is given by Work and Lian [30], who compared the test results of 26 publications that measured the adhesion strength of impact and static ice, showing that adhesion strength decreases with increasing impact velocity. In the study of Work et al., the velocity for static ice was taken as 0 m/s. Because of the slower heat transfer during freezing in low-velocity impacts or static ice formation, the resulting ice exhibits lower stress concentrations on the interface. Although the observed difference in adhesion strength between static and impact ice in this study is slight, it follows the expected trend, backing the assumption that glaze ice generated by the ice printer resembles impact ice generated in the icing wind tunnel rather than static ice.

Adhesion strength measurements for rime ice generated with the ice printer and the icing wind tunnel show minor discrepancies, with slightly lower values observed for the wind-tunnel specimens. However, the ice printer values fall within the interquartile range and whiskers of the icing wind-tunnel data. It is important to note that the rime ice specimens from the icing wind tunnel had a lower mass of 0.75 g, compared to the 1 g of the other specimens. This mass difference is due to technical limitations that prevent longer spray durations in the icing wind tunnel at such a low temperature of −17°C. Although the reduced ice mass is not expected to affect adhesion strength, differences in the crystalline structure of the ice may explain the slight deviation in adhesion strength between the printer and wind-tunnel rime ice. A visual comparison between close-up images (see Fig. 12) of rime ice from the ice printer (right) and the icing wind tunnel (left) reveals differences in their crystalline structure. The crystalline structure's influence on ice adhesion strength has also been demonstrated by Orndorf et al. [40], who found that a bigger grain size corresponds to a lower adhesion strength. However, no definitive conclusions can be drawn about crystal size in this study. Although the slightly higher adhesion strength measured for the printer-generated rime ice could suggest the presence of glaze ice rather than rime ice, this interpretation appears unlikely. One conceivable explanation is the formation of a thin glaze ice layer during the initial moments of the printing process, potentially accounting for the similar adhesion strength observed for rime and glaze ice on printed samples. However, several factors argue against this scenario. Because of the lower thermal conductivity of ice compared to aluminum, heat released during freezing is dissipated most effectively at the beginning of the process, when droplets first contact the cold aluminum substrate, rather than during later deposition on an existing ice layer. Additionally, the directed airflow from the nozzle enhances convective cooling and promotes the removal of latent heat. Under such conditions, if glaze ice formation were already limited at the onset, it would be even less likely to occur in subsequent layers. This aligns with further observations: the printed ice exhibits optical and density characteristics consistent with rime ice, and the printing conditions (low ambient temperature, small droplet size, and low LWC) strongly favor rime ice formation. Nevertheless, the possibility of a thin glaze ice layer cannot be entirely ruled out and should be examined in future work.

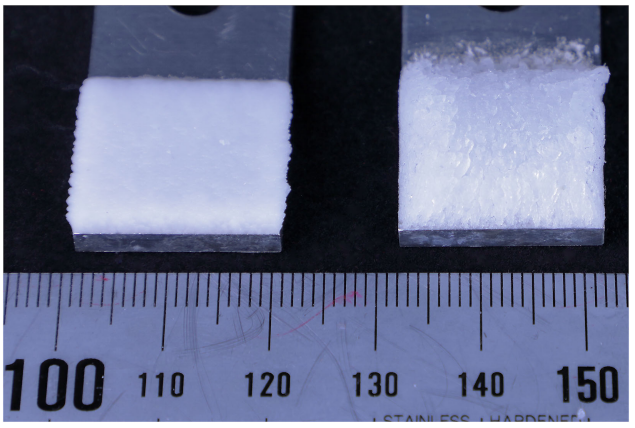

Fig. 12 Rime ice generated with the icing wind tunnel (left) and the ice printer (right).

A general comparison of the adhesion strength measurements with literature values shows that the results obtained in this study are considerably lower for all ice types. Table 5 shows the mean values and standard deviation (SD) of different adhesion strength measurements reported in the literature compared to those from this study. The table also includes the corresponding ice generation methods and ice types used in the other studies. Only studies employing a centrifuge for adhesion testing and conducting tests at an ambient temperature of −10°C are included for comparability. Reported values in the literature range from 242 to 529 kPa for glaze ice, from 348 to 780 kPa for rime ice, and from 284 to 290 kPa for static ice, all significantly higher than the values found in this study. However, the wide range of values and large SD found in the literature observed across these studies highlight the difficulty of comparing adhesion strength data, as numerous parameters influence the results. The reason for the relatively low adhesion strength observed in this study remains unclear. It is considered unlikely that the printer itself is responsible, as specimens generated using both silicone molds and the icing wind tunnel exhibited similarly reduced adhesion values compared to those reported in the literature. The discrepancy is therefore presumed to originate from either the aluminum substrate material or the specifics of the centrifuge setup. Further investigations are required to identify the underlying cause.

Surface roughness [46] and ambient temperature during testing [23,30] have been identified in the literature as major parameters influencing ice adhesion strength. All adhesion tests in this study were performed at a constant ambient temperature of −10°C using identical substrate specimens, minimizing the influence of temperature and surface roughness and enabling consistent comparison across ice types within this study. Differences in icing conditions, particularly the MVD and LWC during ice generation, may still have influenced the results. Soltis et al. [46] report a decrease in adhesion strength with increasing MVD and LWC due to a higher heat transfer and, therefore, surface temperatures slightly above the freezing point during the freezing process. Because the LWC during rime ice generation is notably lower in both the icing wind tunnel and the ice printer, due to higher air pressure, increased nozzle

Table 5 Comparison of adhesion strength measurements of this study with the literature

Researcher	Ice generation method	Ice type	Adhesion strength (mean ± SD)
This study	Ice printer	Glaze ice	75 ± 18 kPa
This study	Icing wind tunnel	Glaze ice	69 ± 15 kPa
Rønneberg et al. [24]	Icing wind tunnel	Glaze ice	529 ± 119 kPa
Laforte and Beisswenger [41]	Icing wind tunnel	Glaze ice	350 ± 63 kPa
Menini and Farzaneh [42]	Icing wind tunnel	Glaze ice	505 ± 65 kPa
Kulinich and Farzaneh [43]	Icing wind tunnel	Glaze ice	360 kPa
Arianpour et al. [44]	Icing wind tunnel	Glaze ice	242 ± 26 kPa
This study	Ice printer	Rime ice	66 ± 13 kPa
This study	Icing wind tunnel	Rime ice	50 ± 7 kPa
Rønneberg et al. [24]	Icing wind tunnel	Rime ice	780 ± 102 kPa
Blackburn et al. [45]	Icing wind tunnel	Rime ice	348 ± 200 kPa
This study	Silicon molds	Static ice	82 ± 3 kPa
Rønneberg et al. [24]	Silicon molds	Static ice	284 ± 83 kPa
Janjua [29]	Silicon molds	Static ice	290 ± 30 kPa

height, and faster printing speed, higher adhesion strength compared to glaze ice would be expected in both the icing wind tunnel and the ice printer. However, this anticipated trend has not been observed. The reason for the glaze ice's higher adhesion strength remains unclear and requires further investigation.

The challenges associated with interstudy comparisons and the factors influencing ice adhesion strength are comprehensively discussed by Rønneberg et al. [24], Work and Lian [30], and Bleszynski and Clark [34]. These studies emphasize that measurements of ice adhesion strength can vary by more than an order of magnitude across different laboratories and testing facilities, primarily due to the lack of standardized procedures for ice generation, test conditions, and data evaluation. Consequently, the comparability of results from different studies is severely limited. For this reason, the primary objective of this study was to compare the obtained values with one another and establish the ice printer as a valuable method to produce impact ice.

VI. Conclusions

This paper introduces the ice printer as a novel method for generating impact ice. The working principle of the ice printer is presented, along with an investigation into how adjustable process parameters influence ice formation. The ice layers produced with the ice printer were compared to those generated with an icing wind tunnel and to static ice formed in silicon molds. The results demonstrate that the ice printer produces ice with comparable density, adhesion strength, and optical properties to those generated with an icing wind tunnel. Although static ice specimens show similar density values, they exhibit higher adhesion strength due to differences in the freezing process. This observation aligns with findings reported in the literature. Based on the results of this study, the ice produced with the ice printer can be classified as impact ice, validating the printer as a cost- and time-efficient alternative for generating impact ice in a laboratory environment.

The homogeneity and comparable reproducibility to that of an icing wind tunnel, combined with the high adjustability of the printing parameters, make the ice printer a valuable addition in the early development stages of deicing and anti-icing systems. The ability to apply controlled individual ice layers simplifies investigations into the influence of ice thickness on such systems. Furthermore, using a regular household freezer instead of a complex freezing chamber to operate the printer facilitates the production of impact ice. Together with its time and cost efficiency, these features make the ice printer a practical and accessible solution for impact ice generation in almost any laboratory setting. As a next step toward broader acceptance of the ice printer as a reliable method for generating impact ice, a round-robin study is planned to compare the ice layers generated with the ice printer to those from various icing wind tunnels.

Acknowledgments

This research was funded by the German Federal Ministry for Economic Affairs and Climate Action under project number 20Y2204B (HYBATS, Hybrid Ice Protection on Advanced Natural Laminar Slat).

References

[1] US Department of Transportation; Federal Aviation Administration, "AC 91-74B - Pilot Guide: Flight In Icing Conditions," 2015.

[2] Deiler, C., and Fezans, N., "Performance-Based Ice Detection Methodology," *Journal of Aircraft*, Vol. 57, No. 2, 2020, pp. 209–223. https://doi.org/10.2514/1.C034828

[3] Federal Aviation Administration, Department of Transportation, "14 CFR Part 25 (Up to Date as of 4/02/2025): Airworthiness Standards: Transport Category Airplanes," 2025, https://www.ecfr.gov/current/title-14/part-25.

[4] Palanque, V., "Design of Low Consumption Electro-Mechanical De-Icing System," Dissertation, Université Fédérale Toulouse Midi Pyrénées, 2022, https://hal.science/tel-03935665/.

[5] Zhang, F., Deng, W., Nan, H., Zhang, L., and Huang, Z., "Reliability Analysis of Bleed Air Anti-Icing System Based on Subset Simulation Method," *Applied Thermal Engineering*, Vol. 115, March 2017, pp. 17–21. https://doi.org/10.1016/j.applthermaleng.2016.11.202

[6] Schwab, A., Thomas, A., Bennett, J., Robertson, E., and Cary, S., "Electrification of Aircraft: Challenges," *Barriers, and Potential Impacts*, National Renewable Energy Lab., TR NREL/TP-6A20-80220, 2021. https://doi.org/10.2172/1827628

[7] Roy, R., Raj, L. P., Jo, J.-H., Cho, M.-Y., Kweon, J.-H., and Myong, R. S., "Multiphysics Anti-Icing Simulation of a CFRP Composite Wing Structure Embedded with Thin Etched-Foil Electrothermal Heating Films in Glaze Ice Conditions," *Composite Structures*, Vol. 276, Nov. 2021, Paper 114441. https://doi.org/10.1016/j.compstruct.2021.114441

[8] European Union Aviation Safety Agency, "Certification Specifications and Acceptable Means of Compliance for Large Aeroplanes (CS-25)," 2021, https://www.easa.europa.eu/en/document-library/easy-access-rules/easy-access-rules-large-aeroplanes-cs-25.

[9] Fikke, S., Ronsten, G., Heimo, A., Kunz, S., Ostrozlik, M., Persson, P.-E., Sabata, J., Wareing, B., Wichura, B., and Chum, J., "COST 727: Atmospheric Icing on Structures Measurements and Data Collection on Icing: State of the Art," *MeteoSchweiz*, edited by MeteoSwiss, Vol. 75, 2006, p. 110.

[10] Gao, L., Liu, Y., Zhou, W., and Hu, H., "An Experimental Study on the Aerodynamic Performance Degradation of a Wind Turbine Blade Model Induced by Ice Accretion Process," *Renewable Energy*, Vol. 133, April 2019, pp. 663–675. https://doi.org/10.1016/j.renene.2018.10.032

[11] Makkonen, L., "Ice Adhesion —Theory, Measurements and Countermeasures," *Journal of Adhesion Science and Technology*, Vol. 26, Nos. 4–5, 2012, pp. 413–445. https://doi.org/10.1163/016942411X574583

[12] Bragg, M. B., Gregorek, G. M., and Lee, J. D., "Airfoil Aerodynamics in Icing Conditions," *Journal of Aircraft*, Vol. 23, No. 1, 1986, pp. 76–81. https://doi.org/10.2514/3.45269

[13] Hansman, R. J., and Kirby, M. S., "Comparison of Wet and Dry Growth in Artificial and Flight Icing Conditions," *Journal of Thermophysics and Heat Transfer*, Vol. 1, No. 3, 1987, pp. 215–221. https://doi.org/10.2514/3.30

[14] Bansmer, S. E., Baumert, A., Sattler, S., Knop, I., Leroy, D., Schwarzenboeck, A., Jurkat-Witschas, T., Voigt, C., Pervier, H., and Esposito, B., "Design, Construction and Commissioning of the Braunschweig Icing Wind Tunnel," *Atmospheric Measurement Techniques*, Vol. 11, No. 6, 2018, pp. 3221–3249. https://doi.org/10.5194/amt-11-3221-2018

[15] Herman, E., "Goodrich Icing Wind Tunnel Overview, Improvements and Capabilities," *44th AIAA Aerospace Sciences Meeting and Exhibit*, AIAA Paper 2006-0862, 2006. https://doi.org/10.2514/6.2006-862

[16] Vecchione, L., De Matteis, P., and Leone, G., "An Overview of the CIRA Icing Wind Tunnel," *41st Aerospace Sciences Meeting and Exhibit*, AIAA Paper 2003-0900, 2003.

[17] Wiedemann, J., Meyer, P., Feder, J., Sinapius, M., Riemenschneider, J., and Hühne, C., "Electromechanical Deicing of Helicopter Structures with Integrated Ice Detection by Impedance Measurement," *Journal of Aerospace Engineering*, Vol. 37, No. 1, 2024. https://doi.org/10.1061/JAEEEZ.ASENG-5131

[18] Rehfeld, N., Brassard, J.-D., Yamazaki, M., Sakaue, H., Balordi, M., Koivuluoto, H., Mora, J., He, J., Pervier, M.-L., Dolatabadi, A., et al., "Round-Robin Study for Ice Adhesion Tests," *Aerospace*, Vol. 11, No. 2, 2024, p. 106. https://doi.org/10.3390/aerospace11020106

[19] Wang, Z., Zhu, C., and Zhao, N., "Experimental Study on the Effect of Different Parameters on Rotor Blade Icing in a Cold Chamber," *Applied Sciences*, Vol. 10, No. 17, 2020, p. 5884. https://doi.org/10.3390/app10175884

[20] Alekseenko, S. V., Mendig, C., Schulz, M., Sinapius, M., and Prykhodko, O. A., "An Experimental Study of Freezing of Supercooled Water Droplet on Solid Surface," *Technical Physics Letters*, Vol. 42, No. 5, 2016, pp. 524–527. https://doi.org/10.1134/S1063785016050187

[21] Tetteh, E., Jeong, M., Loth, E., Cummings, J., and Loebig, J., "Static- vs Impact-Ice-Shear Adhesion on Metals and a Self-Lubricating Icephobic Coating," *AIAA Journal*, Vol. 62, No. 9, 2024, pp. 3448–3462. https://doi.org/10.2514/1.J063427

[22] Tetteh, E., and Loth, E., "Reducing Static and Impact Ice Adhesion with a Self-Lubricating Icephobic Coating (SLIC)," *Coatings*, Vol. 10,

No. 3, 2020, p. 262.
https://doi.org/10.3390/coatings10030262
[23] Chu, M. L., Scavuzzo, R. J., and Srivatsan, T. S., "An Experimental Technique for the Evaluation of Properties of Ice," *Journal of Materials Research*, Vol. 6, No. 9, 1991, pp. 1919–1925.
https://doi.org/10.1557/JMR.1991.1919
[24] Rønneberg, S., Laforte, C., Volat, C., He, J., and Zhang, Z., "The Effect of Ice Type on Ice Adhesion," *AIP Advances*, Vol. 9, No. 5, 2019.
https://doi.org/10.1063/1.5086242
[25] Petrovic, J. J., "Review Mechanical Properties of Ice and Snow," *Journal of Materials Science*, Vol. 38, No. 1, 2003, pp. 1–6.
https://doi.org/10.1023/A:1021134128038
[26] Druez, J., McComber, P., and Tremblay, C., "Experimental Results on the Tensile Strength of Atmospheric Ice," *Transactions of the Canadian Society for Mechanical Engineering*, Vol. 13, No. 3, 1989, pp. 59–64.
https://doi.org/10.1139/tcsme-1989-0010
[27] Rønneberg, S., He, J., and Zhang, Z., "The Need for Standards in Low Ice Adhesion Surface Research: A Critical Review," *Journal of Adhesion Science and Technology*, Vol. 34, No. 3, 2020, pp. 319–347.
https://doi.org/10.1080/01694243.2019.1679523
[28] Schulson, E. M., "The Structure and Mechanical Behavior of Ice," *Journal of the Minerals, Metals & Materials Society (TMS)*, Vol. 51, No. 2, 1999, pp. 21–27.
https://doi.org/10.1007/s11837-999-0206-4
[29] Janjua, Z. A., "The Influence of Freezing and Ambient Temperature on the Adhesion Strength of Ice," *Cold Regions Science and Technology*, Vol. 140, Aug. 2017, pp. 14–19.
https://doi.org/10.1016/j.coldregions.2017.05.001
[30] Work, A., and Lian, Y., "A Critical Review of the Measurement of Ice Adhesion to Solid Substrates," *Progress in Aerospace Sciences*, Vol. 98, April 2018, pp. 1–26.
https://doi.org/10.1016/j.paerosci.2018.03.001
[31] Politovich, M. K., "Predicting Glaze or Rime Ice Growth on Airfoils," *Journal of Aircraft*, Vol. 37, No. 1, 2000, pp. 117–121.
https://doi.org/10.2514/2.2570
[32] Macklin, W. C., "The Density and Structure of Ice Formed by Accretion," *Quarterly Journal of the Royal Meteorological Society*, Vol. 88, No. 375, 1962, pp. 30–50.
https://doi.org/10.1002/qj.49708837504
[33] Vargas, M., Broughton, H., Sims, J. J., Bleeze, B., and Gaines, V., "Local and Total Density Measurements in Ice Shapes," *Journal of Aircraft*, Vol. 44, No. 3, 2007, pp. 780–789.
https://doi.org/10.2514/1.23326
[34] Bleszynski, M., and Clark, E., "Current Ice Adhesion Testing Methods and the Need for a Standard: A Concise Review," *Standards*, Vol. 1, No. 2, 2021, pp. 117–133.
https://doi.org/10.3390/standards1020011
[35] Kasaai, M. R., and Farzaneh, M., "A Critical Review of Evaluation Methods of Ice Adhesion Strength on the Surface of Materials," *Proceedings of the 23rd International Conference on Offshore Mechanics and Arctic Engineering - 2004*, ASME, New York, NY, 2004, pp. 919–926.
https://doi.org/10.1115/OMAE2004-51264
[36] Schulz, M., "Zeitabhängigkeit der Eisadhäsionsfestigkeit," Dissertation, Technische Universität Braunschweig, Braunschweig, 2016.
[37] Palanque, V., Villeneuve, E., Budinger, M., Pommier-Budinger, V., and Momen, G., "Experimental Measurement and Expression of Atmospheric Ice Young's Modulus According to Its Density," *Cold Regions Science and Technology*, Vol. 212, Aug. 2023, Paper 103890.
https://doi.org/10.1016/j.coldregions.2023.103890
[38] Palanque, V., Villeneuve, E., Budinger, M., Pommier-Budinger, V., and Momen, G., "Cohesive Strength and Fracture Toughness of Atmospheric Ice," *Cold Regions Science and Technology*, Vol. 204, Dec. 2022, Paper 103679.
https://doi.org/10.1016/j.coldregions.2022.103679
[39] Rehfeld, N., Speckmann, B., and Stenzel, V., "Parameter Study for the Ice Adhesion Centrifuge Test," *Applied Sciences*, Vol. 12, No. 3, 2022, p. 1583.
https://doi.org/10.3390/app12031583
[40] Orndorf, N., Chen, R.-C., and Work, A., "An Investigation of the Grain Size and Adhesion Strength of High-Speed Impact Ice," NASA/TM-20210014377, 2021.
https://doi.org/10.13140/RG.2.2.18918.96329
[41] Laforte, C., and Beisswenger, A., "Icephobic Material Centrifuge Adhesion Test," *Proceedings of the IWAIS XI*, Montréal, QC, Canada, June 2005, p. 15.
[42] Menini, R., and Farzaneh, M., "Elaboration of Al_2O_3/PTFE Icephobic Coatings for Protecting Aluminum Surfaces," *Surface and Coatings Technology*, Vol. 203, No. 14, 2009, pp. 1941–1946.
https://doi.org/10.1016/j.surfcoat.2009.01.030
[43] Kulinich, S. A., and Farzaneh, M., "On Ice-Releasing Properties of Rough Hydrophobic Coatings," *Cold Regions Science and Technology*, Vol. 65, No. 1, 2011, pp. 60–64.
https://doi.org/10.1016/j.coldregions.2010.01.001
[44] Arianpour, F., Farzaneh, M., and Jafari, R., "Hydrophobic and Ice-Phobic Properties of Self-Assembled Monolayers (SAMs) Coatings on AA6061," *Progress in Organic Coatings*, Vol. 93, April 2016, pp. 41–45.
https://doi.org/10.1016/j.porgcoat.2015.12.008
[45] Blackburn, C., Villeneuve, E., Bakhshandeh, E., Momen, G., Garcia, J., and Noiville, R., "Ice Adhesion Measurements: Assessing the Effect of Icing Conditions," *International Workshop on Atmospheric Icing of Structures*, McGill Univ., Montreal, Canada, 2022, https://www.mcgill.ca/iwais2022/files/iwais2022/paperid052.pdf.
[46] Soltis, J., Palacios, J., Eden, T., and Wolfe, D., "Evaluation of Ice-Adhesion Strength on Erosion-Resistant Materials," *AIAA Journal*, Vol. 53, No. 7, 2015, pp. 1825–1835.
https://doi.org/10.2514/1.J053516

A. Broeren
Associate Editor